ELSEVIER

Journal of Molecular Catalysis A: Chemical 100 (1995) 129–145

JOURNAL OF MOLECULAR CATALYSIS A: CHEMICAL

# Evidence for kinetic and oxidative stabilization of Rh on Mo-promoted $Rh/Al_2O_3$

Eric E. Lowenthal [a], Larry F. Allard [b], Mure Te [a], Henry C. Foley [a,*]

[a] *Center for Catalytic Science and Technology, Department of Chemical Engineering, University of Delaware, Newark, DE 19716, USA*

[b] *Materials Analysis User Center, High Temperature Materials Laboratory, Oak Ridge National Laboratory, P.O. Box 2008, Oak Ridge, Tennessee 37831-6064, USA*

**Abstract**

Carbon monoxide hydrogenation studies on silica- and alumina-supported Rh catalysts conducted in our laboratories as well as those reported in the literature suggest that the addition of early transition-metal oxides to the catalyst surface exerts a promotional influence on active Rh centers. This promotion leads to enhanced oxygenate selectivity. Explanations of the promotional influence of the early transition-metal oxides fall into three categories: (i) kinetic stabilization of small Rh aggregates, (ii) wetting and spreading of the transition-metal oxide, leading to decoration of the surface of Rh crystallites, and (iii) oxidative stabilization of Rh aggregates, altering Rh interactions with sub-carbonyls during reaction. Characterization of the Rh–Mo/$\gamma$-$Al_2O_3$ system provides supporting evidence for both kinetic stabilization and oxidative stabilization of Rh aggregates and suggests that these processes contribute to the enhanced oxygenate selectivity of these materials. Hydrogen and carbon monoxide chemisorption results provide evidence for highly dispersed and oxidatively stabilized Rh aggregates. Even after extended on-stream testing ($>10$ h), where metal aggregation is unavoidable, high-resolution transmission electron microscopy, associated energy dispersive spectroscopy, and the use of fast-Fourier transform post-processing to produce optical diffractograms highlight differences in the metal-aggregate morphology.

*Keywords*: Carbon monoxide; Bimetallic catalysts; Rhodium; Molybdenum; Supported catalysts ; Gamma-alumina; Chemisorption; Surface modification; Hydrogen; Carbon monoxide; High-resolution transmission electron microscopy; Image processing

## 1. Introduction

"To elucidate the modifying mechanism in supported rhodium catalysts prepared via the decomposition of anchored metal complexes, it is necessary to obtain data on the state of supported components. This will be the aim of future studies." So wrote Yermakov and coworkers [1] in 1980 in one of the earliest attempts to understand the influence of promoter metals on supported Rh catalysts. Such early work began to indirectly probe the state of promoter metals, namely Sn, Pb, Mo, and W, through hydrogen chemisorption and temperature-programmed desorption (TPD) experiments as a supplement to hydrocarbon microreactor studies [2]. But this comment by Yermakov correctly anticipated the main emphasis of future investigations of promoted Rh on silica and alumina.

Investigations in our laboratories and elsewhere have demonstrated that the oxygenate selectivity of silica- and alumina-supported Rh catalysts is

* Corresponding author. tel. (+1-302) 8316856, fax. (+1-302) 8312085, e-mail: foley@che.udel.edu


*SSDI* 1381-1169(95)00177-8

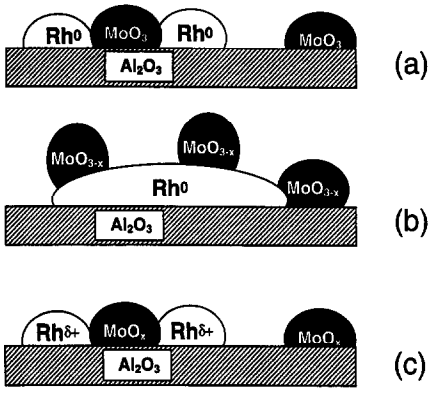


Fig. 1. The three main paradigms for the promotional influence of Mo on supported Rh: (a) kinetic stabilization, (b) metal–oxide decoration, and (c) oxidative stabilization.

enhanced through the use of early transition-metal promoters in the CO hydrogenation system [3–21]. Within the more narrow subset of Mo-promoted Rh catalysts supported on $SiO_2$ and $Al_2O_3$ (where strong metal–support interactions are thought to be minimal), previous investigations can be grouped by the three main explanations put forth for the influence of Mo on the active Rh centers. These three explanations are schematically represented in Fig. 1.

The first paradigm for Mo promotion argues that Mo, in the form of an oxide, kinetically stabilizes Rh in smaller, site-isolated aggregates and inhibits the sintering of these aggregates in the high-temperature CO hydrogenation environment (Fig. 1a). The second paradigm suggests a grafting process wherein the molybdenum oxide decorates the surface of the Rh aggregates (Fig. 1b) leading to smaller ensembles of exposed metal sites and perhaps some weak chemisorptive interaction between the oxygen in Rh sub-carbonyls and this molybdenum oxide adlayer during CO hydrogenation. The third paradigm argues that molybdenum oxide, when present in intimate contact with Rh, slightly oxidizes the Rh through some weak, dative electron transfer from the Rh towards the molybdenum oxide (Fig. 1c) and, hence, alters the nature of the active Rh centers' interactions with adsorbed carbonyls. Note that the catalyst preparation methods and the transition-metal loadings in these studies vary considerably. The various catalyst studies and associated references supporting these models are revisited in connection with a brief set of unifying observations set forth in the last section of this paper.

Carbon monoxide hydrogenation results summarized herein reaffirm the enhanced oxygenate selectivity and activity of a series of Mo-promoted, alumina-supported Rh catalysts. Based upon chemisorptive analysis and high-resolution transmission electron microscopy (HRTEM), this investigation supports *both the kinetic stabilization and the oxidative stabilization of rhodium* in near atomic form in the presence of molybdena. HRTEM and associated fast-Fourier transform (FFT) analysis reveal no direct evidence for the decoration of Rh aggregates by a molybdenum oxide adlayer. Furthermore, comparisons between room-temperature $H_2$ and CO chemisorption on these materials point towards an oxidative interaction between the Rh and the molybdena rather than a metal–oxide grafting process. Finally, some unifying ideas are suggested about the controversial role of molybdena. These ideas are based, in part, on the nature of the synthesis techniques employed by various investigators.

## 2. Methods

### 2.1. Catalyst synthesis

The catalysts synthesized in this study were prepared via sequential chemisorption of homogeneous, transition-metal carbonyls on $Al_2O_3$ in a non-aqueous slurry of anhydrous heptane (99 + % pure, Aldrich) under a nitrogen atmosphere. Two groups of catalysts are discussed in this context: a monometallic series of $Rh/\gamma\text{-}Al_2O_3$ and a similarly loaded, bimetallic series of $Rh\text{–}Mo/\gamma\text{-}Al_2O_3$ with a roughly constant Mo loading. Table 1 summarizes the samples for which reaction and characterization data are presented. All of the metal loadings reported in Table 1 are based on elemental analysis. The monometallic catalysts were synthesized by chemisorbing $Rh(CO)_2(acac)$ (Strem) on the surface of $\gamma\text{-}Al_2O_3$ (American Cyanamid, BET S.A. = 250

Table 1
Transition metal loadings of mono- and bimetallic catalyst series

| Catalyst [a] | Rh wt% | Mo wt% | Rh/Mo Ratio |
|---|---|---|---|
| Rh–II | 0.45 | – | |
| Rh–III | 1.37 | – | |
| Rh–IV | 2.66 | – | |
| RhMo–II | 0.41 | 1.42 | 0.27 |
| RhMo–III | 1.21 | 1.46 | 0.77 |
| RhMo–IV | 2.43 | 1.23 | 1.84 |

[a] All the catalysts in this series are supported on $\gamma$-$Al_2O_3$ (BET S.A. = 250 $m^2/g$).

$m^2/g$) and subsequently filtering, drying, and mildly calcining the resulting solid in air at 120°C overnight. The bimetallic series were synthesized by first preparing a batch of Mo/$\gamma$-$Al_2O_3$ with a constant metal loading by slurring the $\gamma$-$Al_2O_3$ with $Mo(CO)_6$ (Strem) and subsequently filtering and drying the resulting solid in air. Samples of the resulting Mo/$\gamma$-$Al_2O_3$ material were then placed in fresh slurries, $Rh(CO)_2(acac)$ was sequentially chemisorbed on the catalyst surface, and the resulting bimetallic materials were filtered, dried, and mildly calcined in air at 120°C overnight. Additional details on the catalyst synthesis have been described elsewhere [10,22].

### 2.2. Microreactor testing

CO hydrogenation reactions were performed in a fixed bed, down-flow, high-pressure microreactor system. Essentially, the microreactor system is composed of (i) a gas delivery system which feeds ultra high-purity CO (Matheson, 99.9 + % pure) and $H_2$ (Matheson, 99.999 + % pure) gases through a series of traps to remove residual $H_2O$, $O_2$ and $Fe(CO)_5$, (ii) a stainless-steel, tubular reactor with a capacity of 0.2–2.0 g of catalyst which is maintained at high pressure through the use of a downstream, back-pressure regulator, and (iii) an on-line product analysis unit composed of two gas chromatographs (Hewlett Packard, models 5730A and 5700A) equipped with thermal conductivity and flame ionization detectors, respectively. Additional details describing the microreactor system have been previously reported [10,20].

All of the CO hydrogenation results summarized herein are from experiments conducted at 300°C and 300 psia (2.0 MPa), with a mole ratio of $CO/H_2 = 1$ and a GHSV = 3500 $h^{-1}$. The catalysts were reduced in flowing $H_2$ for 3 h at 300°C before introducing the reactant mixture. Results which compare activity and selectivity of the various samples are based on the steady-state behavior of the catalysts after 10 h on-stream.

### 2.3. Chemisorption analysis

The chemisorption analysis was conducted in a volumetric chemisorption apparatus, which measured total adsorbent uptakes via changes in adsorbate pressure in a gas manifold of calibrated volume. Each experiment employed 0.450–0.550 g of catalyst, sieved to 45 × 60 mesh ( ~ 290 $\mu$m in diameter) and loaded in a ~ 1/4 in. O.D. Pyrex sample holder. Note that the gas manifold is constructed of Pyrex to avoid significant adsorption of probe molecules on the manifold surface.

For the purpose of reducing the catalyst samples, Grade-5 $H_2$ (AIRCO, 99.999 + % pure) was fed through the apparatus in a down-flow configuration at 50 sccm. Similarly, Matheson Grade CO (99.99 + % pure) was fed through the apparatus to investigate the high-temperature influence of CO on the sample surface as described below. The CO (as well as the $H_2$) used for high-temperature treatment of the samples was delivered to the chemisorption manifold via copper tubing, to avoid $Fe(CO)_5$ contamination. In contrast, research-grade $H_2$ (Matheson, 99.9999 + % pure) and CO (Matheson, 99.99 + % pure) adsorbent gases were employed to measure room temperature gas uptakes, following heating and evacuation of the samples. These gases were delivered to the glass manifold and sample holder via a separate probe-gas manifold which was routinely evacuated to $< 3.0 \times 10^{-5}$ Torr up to the cylinder head. The pressure measurements recorded during the chemisorption experiments were provided by a low-pressure ion gauge (Leybold–Heraeus,

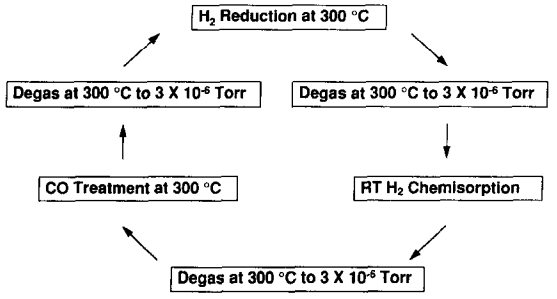


Fig. 2. Schematic cycle of the dynamic chemisorption experiments.

model IM210D) and a pressure transducer and readout (MKS, type 127 and model PDRC-1C) capable of measuring pressures from 0.0–1000.0 Torr with an accuracy of $\pm 0.1$ Torr. This pressure transducer was used to measure adsorbent pressure drops associated with chemi- and physisorption of the probe molecules.

The chemisorption results presented herein stem from two distinct sets of experiments: dynamic chemisorption analysis and room-temperature CO chemisorption. The dynamic chemisorption data were also recorded using static, volumetric techniques; these data are dynamic *with regard to high temperature reactive gas exposure*, namely high-temperature CO. Fig. 2 presents a schematic cycle of the dynamic chemisorption experiments. Stepping through one turnover of this schematic cycle: (i) the sample was reduced in flowing $H_2$ at 300°C for $\geq 30$ min, (ii) the sample was evacuated at 300°C for 30 min and cooled to room temperature to an ultimate vacuum of $<3.0\times10^{-6}$ Torr, (iii) the total, room-temperature $H_2$ uptake was measured to determine the fraction of exposed Rh sites capable of dissociatively adsorbing $H_2$, (iv) the sample was again evacuated at 300°C for 30 min, and (v) 50 sccm of CO was passed over the sample at 300°C for increasing intervals of from 5 to 30 min. Hence, by turning this cycle over repeatedly and monitoring the cumulative exposure to high-temperature CO with each turnover, the H/Rh ratio—a measure of dispersion—could be delineated as a function of reactive gas exposure.

Both the room-temperature $H_2$ chemisorption step of the dynamic chemisorption experiments and the, separate, room-temperature CO chemisorption experiments were carried out by measuring the equilibrium uptakes of the adsorbent at three pressures and extrapolating this isotherm back to zero pressure to extract the total chemisorption (as opposed to physisorption) of the adsorbate on the surface. Equilibrium was determined by monitoring the drop in pressure in the apparatus manifold until no further uptake was recorded. This definition of equilibrium amounted to $\geq 4$ h for each of three room-temperature $H_2$ uptake measurements and $\geq 6$ h for each of three room-temperature CO uptake measurements. No effort was made to distinguish between reversibly and irreversibly adsorbed probe molecules; rather, the total H/Rh or CO/Rh was determined. $H_2$ was assumed to dissociate to atomic hydrogen upon adsorption at active metal centers on the catalyst surface.

X-ray photoelectron spectroscopic (XPS) analysis presented elsewhere [10] and microreactor studies from the literature [19] suggest that for reduction temperatures below 450°C, Mo should be present as a stable oxide on the catalyst surface. The work of Scott and coworkers on the Ru–Mo/$Al_2O_3$ system demonstrated that Mo/$Al_2O_3$ was inactive for $H_2$ or CO chemisorption [23]. Decanio and Storm, in their investigations of the Rh–Mo/$Al_2O_3$ system, found that the adsorption of CO on Mo/$Al_2O_3$ was insignificant below loadings of 8 wt% Mo [11]. Chemisorption testing carried out in our laboratories on 1.43% Mo/$Al_2O_3$ supports these previous findings; no $H_2$ or CO chemisorption was detected when this sample was exposed to the same reduction protocol applied to the mono- and bimetallic Rh samples. Hence, in assessing $H_2$ and CO uptake measurements, Rh was assumed to be the only active phase chemisorbing these probe molecules.

### 2.4. HRTEM, EDS, and fast-Fourier transform analysis

All of the electron micrographs presented were produced using a 200 kV, Hitachi HF-2000 Field Emission TEM (FE-TEM) located in the Materials Analysis User Center of the High Tempera-

ture Materials Laboratory at Oak Ridge National Laboratory (ORNL). The HF-2000 employed in this investigation has a point resolution of approximately 0.23 nm and is equipped with a slow-scan, 1024 × 1024 pixel, CCD camera (Gatan Inc., Model 694) to allow for digital acquisition, processing and analysis of images.

While the HF-2000 is capable of producing probe sizes as small as 1 nm in 'analysis' mode (both condenser lenses excited), the energy dispersive spectroscopy (EDS) presented herein was carried out in the normal imaging or 'zoom' mode. Only the first condenser lens is operative in this mode, and the analytical spot size is about 2.5 nm at cross-over. This larger spot size minimized the severe knock-on heating and radiolytic reduction of the underlying alumina support which often resulted in the loss of the heavy metal particles of interest when the finer spot sizes were employed.

In connection with the CCD camera, micrographs were digitally acquired using Digital-Micrograph 2.5 (Gatan Inc.) image acquisition and processing software. The post-processing and fast-Fourier transform (FFT) analysis of the micrographs were performed using NIH Image 1.57 and Image 1.28b6 (National Institute of Health) image processing software. Particle sizes were calculated by measuring the areas of projected domains of high contrast and atomic fine structure on electron-transparent regions of the specimen using NIH Image 1.57 and calculating the diameter for hypothetical, spherical particles with the same projected area. Datye and Smith [24] have noted that the boundaries of projected domains of high-contrast associated with transition-metal enrichment can be affected by the specimen orientation and the extent of objective lens defocusing. Nevertheless, in the absence of EDS-calibrated, holographic analysis which would distinguish transition-metal boundaries or high-resolution, energy-filtered imaging, such measurements may be the best HRTEM approach to estimating nano-scale particle sizes.

The FFT analysis of indicated image areas produced the equivalent of optical diffractograms from digitally-stored spatial information. The interpretation of the optical diffractograms produced in this fashion is similar to that applied to electron diffraction patterns. FFT analysis of digital images offers advantages over electron diffraction analysis when working with beam-sensitive materials or selecting small specimen areas for evaluation, though certain limitations of this approach must be recognized [25]. The image area masking indicated on various micrographs represents a smooth Gaussian transition to 0 intensity at the borders of these areas; the transition region has been set to 20% of the pixel width of the selected area used for FFT processing. Masking in the spatial domain (i.e., the image) prevents the formation of sharp edge discontinuities otherwise generated upon creation of the periodic extension of an image area used for FFT processing [26]. Such masking, then, prevents the appearance of a dominant, cross-shaped signature in the frequency domain arising from these edge discontinuities. Measurements made on the diffraction spots of the power spectra (i.e., the FFTs) follow the method of Cao and Allard [27]. This method provides a direct correlation between pixel-based distances, measured on computer-generated power spectra, and crystalline *d*-spacings which appear as lattice fringes in the spatial domain.

## 3. Results and discussion

### *3.1. CO hydrogenation testing*

Previous research conducted in our laboratories examined a broad matrix of temperatures and pressures and generated explicit details on the catalyst stabilities and product distributions for the materials described in Table 1 [20]. Table 2 summarizes the core microreactor results from this earlier investigation. The total oxygenate selectivity (including methanol, ethanol, dimethyl ether, and methyl ethyl ether selectivities) was significantly higher on the Mo-promoted samples (see, for example, 41.2% for RhMo–III versus 8.6% for Rh–III). The product distribution

Table 2
CO Hydrogenation product distributions

| Catalyst | $\Sigma C_1$–$C_6$ [a] (%) | $\Sigma$ Oxy [a,b] (%) | CO conv. [c] (%) | TOF |
|---|---|---|---|---|
| Rh–II | 93.3 | 6.7 | 1.59 | $6.77\times10^{-3}$ |
| RhMo–II | 61.8 | 38.2 | 1.08 | $4.36\times10^{-2}$ |
| Rh–III | 91.4 | 8.6 | 4.36 | $7.62\times10^{-3}$ |
| RhMo–III | 58.8 | 41.2 | 1.53 | $6.30\times10^{-2}$ |
| Rh–IV | 91.1 | 6.7 | 7.28 | $8.53\times10^{-3}$ |
| RhMo–IV | 64.6 | 25.6 | 3.69 | $4.82\times10^{-2}$ |

[a] $\Sigma$ indicates total selectivity for the products indicated: $C_1$–$C_6$ = alkanes and olefins up to $C_6$; Oxy = oxygenates, including methanol, ethanol, dimethyl ether, and methylethyl ether.
[b] Excludes $CO_2$ selectivity.
[c] CO conversions were kept below 10% to preserve differential reactor conditions.

on the monometallic catalysts was shifted towards the formation of $C_1$ to $C_6$ alkanes and olefins (Fischer–Tropsch products). In addition, the turnover frequency (TOF), a measure of catalyst activity scaled by the number of active sites determined by $H_2$ chemisorption, was roughly six- to eight-fold higher on the bimetallic samples than on the monometallic samples.

Two other conclusions from these microreactor investigations bear review. First, as Table 2 indicates, the TOFs for the monometallic samples are quite similar, suggesting a similarity in the nature of the active sites on these materials. The same point can, likewise, be made about the bimetallic catalysts, but the dramatic increase in TOFs on the bimetallic materials suggests the presence of active sites which are distinct from those present on the monometallic materials. Second, the catalyst with the highest oxygenate selectivity amongst those examined, RhMo–III, has a Rh/Mo ratio closest to parity (0.77). Here, the Rh and $MoO_x$ are statistically most likely to be in intimate contact. Such intimate contact has been cited as a prerequisite for the formation of integrated, bimetallic crystallites in Rh–Mo catalysts synthesized from organometallic, heteronuclear precursors [12,13]. This intimate contact may be associated with the stabilization of Rh(I) by molybdena during CO hydrogenation.

### 3.2. *Rh gem-dicarbonyl formation and catalyst dispersion*

Signature infrared bands for Rh gem-dicarbonyls ($Rh(I)(CO)_2$) are routinely evaluated as a measurement of Rh dispersion on the silica or alumina support surface. The enhancement of such infrared signatures on Mo-promoted Rh catalysts has been noted to bolster the ideas that molybdena both (i) kinetically stabilizes Rh in small aggregates and (ii) oxidatively (electronically) stabilizes Rh(I) species in the presence of CO [8,19–21]. It is well known from the automotive catalysis literature [28], as well as careful infrared spectroscopic analysis of CO adsorbed on supported Rh catalysts [29–32], that in a high-temperature ($\geq$200°C) reactive atmosphere, atomically dispersed Rh can migrate across the alumina and silica surface through the formation of $Rh(I)(CO)_2$. Indeed, Zaki and coworkers [33], indirectly tracked the growth of Rh aggregates on the alumina surface stemming from cycled CO adsorption and $H_2$ reduction by monitoring the intensity of the infrared signature for gem-dicarbonyls relative to the intensity of bands representative of linear and bridging carbonyl species.

The migration of gem-dicarbonyl species may occur through interaction with surface hydroxyl groups common on high surface area supports (see Fig. 3) or, as intimated by the molecular orbital calculations of Keyes and Watters [34], via migration between 2-O and 3-O coordinate oxyanions. In a approach similar to the use of early transition metal oxides as kinetic stabilizers, researchers in the laboratories of Yates sought to stem the migration of Rh gem-dicarbonyls through both (i) potassium functionalization [35] and (ii) halosilination [36] of surface hydroxyls on alumina. The dynamic chemisorption analysis applied to the monometallic and bimetallic samples investigated in this study capitalizes on this tendency of Rh to migrate in the presence of high-temperature CO. But the influence of molybdena on Rh migration—rather than potassium ion-exchange or surface silination—

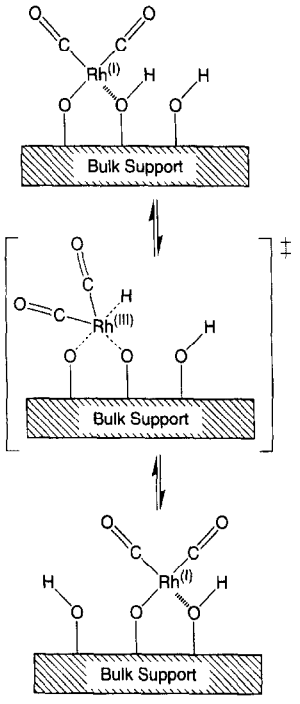


Fig. 3. Hydroxyl-mediated migration of Rh gem-dicarbonyl.

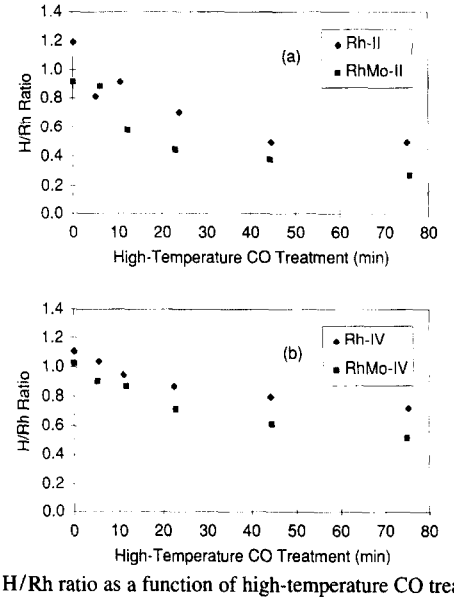


Fig. 4. H/Rh ratio as a function of high-temperature CO treatment: (a) Rh–II and RhMo–II and (b) Rh–IV and RhMo–IV.

has been explored. Through a series of cycled, high-temperature gas treatments and room-temperature chemisorption measurements, the dispersion of the Rh active centers on both the monometallic and bimetallic samples has been mapped out as a function of exposure to high-temperature CO.

Fig. 4 compares the reorganization of the Rh–II and RhMo–II samples (Fig. 4a) and the Rh–IV and RhMo–IV samples (Fig. 4b) over a period of 75 min of high-temperature CO exposure. The data in Fig. 4 demonstrate that the H/Rh is consistently lower for the bimetallic samples, and the fraction of exposed active sites decreases monotonically with cycled exposure to CO and reduction in $H_2$ at 300°C. On RhMo–II and RhMo–IV, then, the presence of molybdena does not appear to exert any *dramatic* kinetic stabilization effect on the rhodium atoms and aggregates which are sensitive to $H_2$ chemisorption at room temperature. Furthermore, a fraction of Rh sites in the Mo-promoted materials have had their ability to dissociatively adsorb $H_2$ at room temperature altered—as evidenced by consistently lower uptakes—either through oxidative stabilization or surface coverage of the Rh or some other phenomena. In contrast, Fig. 5 distinguishes the precipitous reorganization of the catalyst surface on monometallic Rh–III from the relatively stable, though lower, dispersion seen on RhMo–III. This distinction is particularly evident in Fig. 5(b), where the surface reorganization has been monitored over approximately 4 h, whichroughly cor-

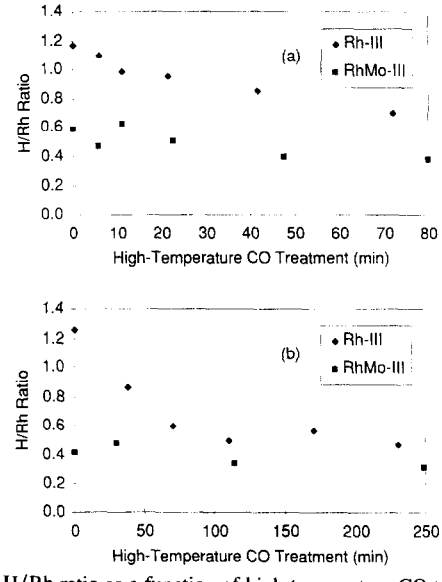


Fig. 5. H/Rh ratio as a function of high-temperature CO treatment for Rh–III and RhMo–III: (a) total high-temperature CO exposure of less than 80 min and (b) total high-temperature CO exposure of approximately 4 h.

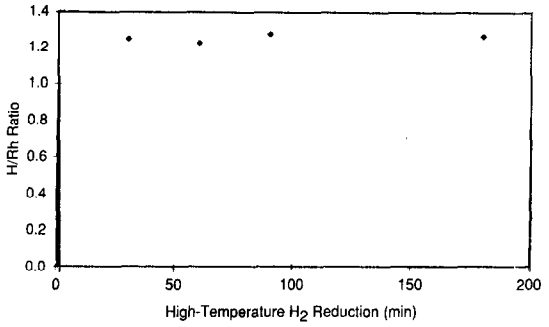


Fig. 6. H/Rh Ratio as a function of high-temperature $H_2$ reduction for Rh–III.

responds to the period during which the activity of these catalyst dropped most severely during stability testing reported previously [20]. Here, the molybdena in RhMo–III, the catalyst which microreactor studies identified as the most selective for the production of oxygenated products, appears to stabilize the Rh atoms and aggregates sensitive to $H_2$ chemisorption in a moderately dispersed array. In addition, both Fig. 5a and Fig. 5b demonstrate that RhMo–III has a consistently lower H/Rh than Rh–III, once again suggesting either some sustained oxidative or occlusive interaction between the molybdena and a fraction of Rh sites ( $\approx 40\%$) on the support surface.

Implicit in the dynamic chemisorption results presented thus far is the assumption that high-temperature $H_2$ exposure alone was not responsible for the migration and agglomeration of the active Rh sites on these catalysts. It was determined that 30 min of exposure to flowing $H_2$ effectively reduced all the samples analyzed in this study. In addition, the sintering influence of high-temperature $H_2$ exposure was probed directly for several of the monometallic and bimetallic samples. Fig. 6 presents results for a representative sample, Rh–III, and depicts the H/Rh ratio implied by room-temperature uptake measurements on this sample following successive high-temperature $H_2$ reduction cycles. As Fig. 6 demonstrates, prolonged and repeated $H_2$ reduction alone was not responsible for agglomeration or loss of active site density in these materials with maximum temperature exposures of 300°C.

### 3.3. Room-temperature CO chemisorption

Table 3 summarizes and compares the $H_2$ and CO chemisorption results for room-temperature uptake measurements following catalyst reduction but prior to any extended high-temperature gas treatment. The prominence of gem-dicarbonyl infrared bands, following in situ CO chemisorption, on the bimetallic samples in Table 3 has been reported elsewhere [20]. Gem-dicarbonyl formation on the RhMo–II and RhMo–III samples appears particularly evident upon comparison of the H/Rh and CO/Rh ratios for these samples; CO adsorbs in a roughly 2:1 ratio to the sites sensitive to $H_2$ chemisorption. The higher Rh loading on RhMo–IV (2.43 wt%, compared to 1.21 wt% for RhMo–III) has still produced a well dispersed catalyst, as measured by $H_2$ chemisorption on this material. But these sites are clearly less prone to adsorb CO in a dicarbonyl mode as evidenced by the lower CO/Rh ratio of 1.1 on RhMo–IV. For the monometallic sample with the lowest loading, Rh–II (0.45 wt% Rh), the catalyst on which Rh is most likely to be atomically dispersed, we see quantitative support for dicarbonyl adsorption of CO in the CO/Rh ratio of 1.8. This ratio falls on the unpromoted Rh catalysts as the loading increases in Rh–III and Rh–IV, pointing towards a decrease in atomically dispersed Rh which is thought most likely to adsorb CO in a gem-dicarbonyl mode. Again, this result agrees with previously presented infrared analysis on these samples which demonstrated an increasing

Table 3
Comparison of room-temperature $H_2$ and CO chemisorption

| Catalyst | H/Rh ratio [a] | Co/Rh ratio [a] |
|---|---|---|
| Rh–II | 1.2 | 1.8 |
| Rh–III | 1.2 | 1.7 |
| Rh–IV | 1.1 | 1.3 |
| RhMo–II | 0.9 | 2.0 |
| RhMo–III | 0.6 | 1.3 |
| RhMo–IV | 1.0 | 1.1 |

[a] Chemisorption ratios represent room-temperature measurements after reduction but prior to any high-temperature, cycled gas treatment.

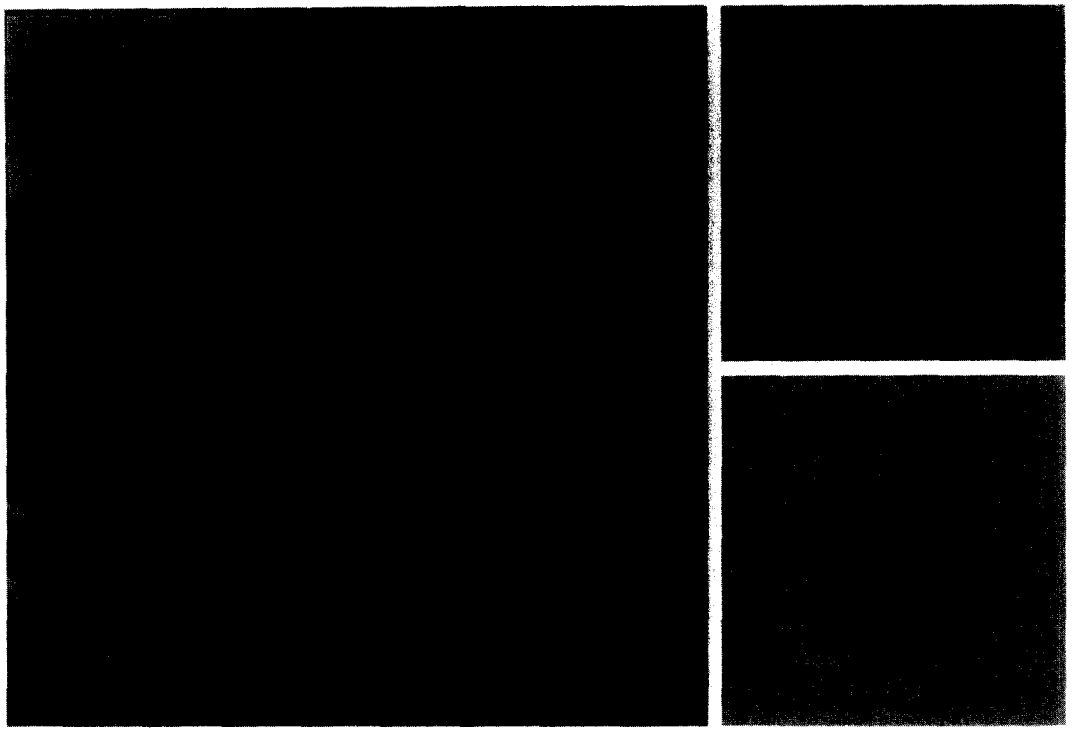

Fig. 7. Rh aggregate formed on Rh–III after > 10 h on-stream for CO hydrogenation. FFTs of the indicated image areas contrast the extent of atomic ordering in the spatial domain: (1) alumina support and (2) lattice fringes of the Rh aggregate. The *d*-spacings indicated are associated with the Rh crystal spacings imbedded in the image information.

prevalence of bridging and linear carbonyls bands relative to gem-dicarbonyl bands with increasing metal loading [20].

The data in Table 3 again emphasize, as mentioned in connection with the dynamic chemisorption measurements, that the fraction of sites active for room-temperature $H_2$ adsorption is consistently lower for the bimetallic samples than for the monometallic samples. This drop in chemisorption is neither consistent nor as prevalent in the case of CO adsorption. The difference in the nature of $H_2$ and CO adsorption suggests that the molybdena stabilizes Rh(I), the gem-dicarbonyl bonding site, on the bimetallic samples and, hence, points to a dative, oxidative interaction from the Rh towards the molybdena which, while promoting CO adsorption, undermines rhodium's ability to dissociatively adsorb $H_2$.

### *3.4. High resolution imaging and analysis*

Catalyst samples which had been exposed to cycled, high-temperature CO and $H_2$ gas treatments were examined by HRTEM. Small domains (0.1–0.3 nm) of high contrast were identified on electron transparent regions of the alumina support in these materials and suggested the presence of sub-nanometer, transition-metal particles. These high-contrast regions were examined via energy dispersive spectroscopy (EDS) aimed at differentiating them from the underlying, alumina support. Due, in part, to the prevalence of knock-on heating and radiolytic reduction of the alumina surface, as well the approach to the limit of the point resolution of the instrument, it was not possible to unambiguously associate these domains with transition metals using the HF-2000 FE-TEM.

In samples which had been tested for CO hydrogenation for > 10 h on-stream, and on which Rh migration was substantial, HRTEM analysis identified well-defined, transition-metal particles. As direct access to electron microscopy facilities at ORNL was not unlimited, HRTEM evaluations of the samples described in Table 1 centered on Rh–

Fig. 8. Rh aggregate formed on Rh–IV after > 10 h on-stream for CO hydrogenation. FFTs of the indicated image areas contrast the extent of atomic ordering in the spatial domain: (1) alumina support and (2) lattice fringes of the Rh aggregate. The *d*-spacings indicated are associated with the Rh crystal spacings imbedded in the image information.

III, Rh–IV, RhMo–III, and RhMo–IV. Note that no detailed HRTEM analysis has been applied to Rh–II and RhMo–II to date. Nevertheless, we believe that distinctions identified between the monometallic and the Mo-promoted samples would be qualitatively preserved in these remaining samples.

As might be anticipated on the monometallic Rh samples, extended testing in the reactive CO hydrogenation environment leads to the formation of large Rh crystallites. Fig. 7 and Fig. 8 present examples of Rh aggregates formed on Rh–III and Rh–IV, respectively. In both micrographs, the presence of well-resolved lattice fringes point to the atomic ordering in these aggregates. This atomic ordering has been further confirmed through the FFT analysis presented in the figures. In the FFT (equivalent to an optical diffractogram) derived from area 1 of both figures, no distinct diffraction spots are present, indicating that area 1 reflects image details associated with only the amorphous nature of the $\gamma$-$Al_2O_3$, rather than those associated with its semi-crystalline, spinel structure. In contrast, the power spectra of area 2 of Fig. 7 and Fig. 8 contain distinct diffraction spots which may be interpreted analogously to the spots present in an electron diffraction pattern. The planar spacings represented by these spots are indicated on the FFTs and, allowing for crystal size and shape effects which may be present in these small aggregates [37,24], agree well with the (111) and (200) planar spacings (2.20 Å and 1.90 Å, respectively) in crystalline Rh (fcc, $a = 3.8031$ Å).

Well-defined, atomically ordered Rh aggregates also were formed on the RhMo–III and RhMo–IV samples. Fig. 9 and Fig. 10 depicted representative particles on these samples. Once again, the FFT analysis underscores the atomic ordering in these particles, compared to the amorphous patterns presented for adjacent areas of the alumina support. Here, again, the planar spacings associated with the diffraction spots on the FFTs agree well with the (111) and (200) spacings for

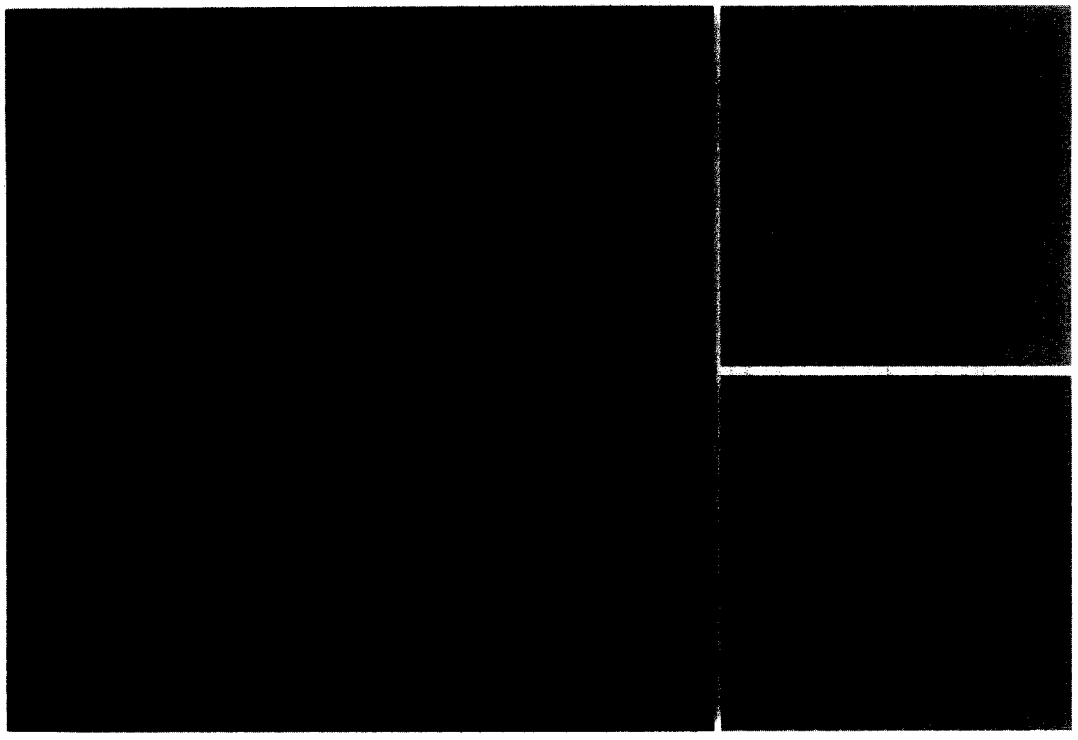

Fig. 9. Rh aggregate formed on RhMo–III after > 10 h on-stream for CO hydrogenation. FFTs of the indicated image areas contrast the extent of atomic ordering in the spatial domain: (1) crystalline Rh aggregate and (2) alumina support. The *d*-spacings indicated are associated with the Rh crystal spacings imbedded in the image information.

crystalline Rh. In particular, based on the *d*-spacings and symmetry of the FFT for area 2 in Fig. 10, this diffractogram can be reasonably assigned to the diffraction pattern observed for the [110] plane of Rh.

Logan and coworkers have demonstrated that careful HRTEM analysis of $Rh/TiO_2$ can resolve the growth of titania adlayers on the surface of Rh crystallites [38]. In the case of the bimetallic samples investigated via HRTEM in this study, *no evidence* for migration of molybdena or associated decoration of Rh crystallites by molybdena was observed. Rather, the direct imaging of particles on the bimetallic samples, as well as the associated FFT analysis, suggests that, like the monometallic samples, the observed crystallites are composed of ordered assemblies of Rh atoms. Furthermore, were molybdena prone to migrate on the support surface, some isolated $MoO_x$ aggregates might have been expected which could have been fingerprinted by EDS. No such molybdena aggregates were observed.

HRTEM analysis of the bimetallic samples suggested a dearth of such ordered particles, since finding them isolated on the alumina support required considerably more searching at 500k× magnification than on the monometallic samples. On a more quantitative basis, the particle size measurements presented in Table 4, suggest that, albeit for a small population of observations, the particles are smaller on the bimetallic samples than on the monometallic samples. Notable in Table 4 was the large median particle size observed on Rh–III. Since the number of observations (the population sample size) was particularly small on this material, emphasis on the exact value of this entry would be inappropriate. Nevertheless, the observation of particles as large as 100 Å in diameter on Rh–III underscores the tendency of Rh to migrate and agglomerate in the absence of a kinetically stabilizing promoter like molybdena.

Since the particles observed on both the monometallic and bimetallic samples appear to be Rh

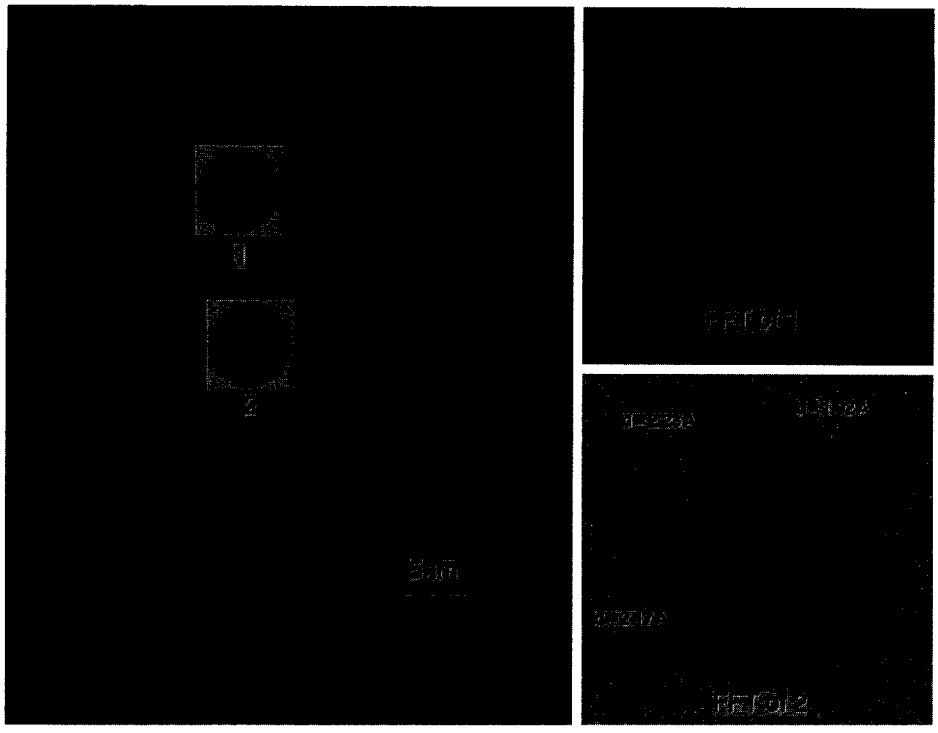

Fig. 10. Rh aggregate formed on RhMo–IV after > 10 h on-stream for CO hydrogenation. FFTs of the indicated image areas contrast the extent of atomic ordering in the spatial domain: (1) alumina support and (2) crystalline Rh aggregate. The FFT of area (2) portrays the diffraction pattern for the [110] Rh crystal plane.

aggregates, some explanation for the location of the molybdena promoter in the bimetallic samples must be provided. While a dearth of atomically ordered crystallites has been reported for the bimetallic samples in this investigation, amorphous areas of high contrast, positively associated with transition-metal enrichment, were quite common. Area B in Fig. 11 is one such area of transition-metal enrichment. The associated energy dispersive spectra in Fig. 12 demonstrate that area B of Fig. 11 is enriched in both Rh and Mo relative to adjacent regions of the support (areas A and C). Yet the FFT analysis of this enriched area, presented in Fig. 13, demonstrates that the region lacks the atomic ordering seen in the Rh aggregates on the same sample (compare the FFT analysis of Fig. 9). This amorphous region of transition-metal enrichment represents the sort of metal–aggregate structure which could account for the intimate contact and oxidative stabilization between Rh and molybdena that was implied by the chemisorptive analysis of the bimetallic samples. The prevalence of this type of disordered, transition-metal structure may be correlated with the enhanced activity and oxygenate selectivity observed on the bimetallic samples during CO hydrogenation.

## 4. Conclusions

### 4.1. Investigation summary

Microreactor results summarized herein reaffirm the enhance activity and superior oxygenate selectivity on Mo-promoted $Rh/\gamma\text{-}Al_2O_3$. The addition of Mo to the catalyst surface effects a shift in the product distribution from Fischer–Tropsch towards oxygenated products. Analysis of the TOFs amongst the catalyst materials discussed suggests the presence of distinct sites on the promoted materials which appear to be absent on the monometallic Rh samples.

Table 4
Summary of particle sizes from HRTEM

| Catalyst | Measurements [a] | Median particle diameter (Å) [b] |
|---|---|---|
| Rh–III | 5 | 61 |
| RhMo–III | 11 | 29 |
| Rh–IV | 10 | 37 |
| RhMo–IV | 24 | 31 |

[a] 'Measurements' represent the number of observed particles upon which the median is based.
[b] Due to the small sample size, median rather than average particle size is reported.

Dynamic chemisorption measurements provide several insights into catalyst behavior. First, tracking the H/Rh ratio as a function of high-temperature CO exposure highlights the surface reorganization of Rh which occurs in the reactive CO hydrogenation environment. Mo-promotion, when closest to parity with the Rh loading, not only produces the most selective oxygenate catalyst, but also retards the surface migration of Rh. That is, the molybdena kinetically stabilizes the Rh sites active for $H_2$ chemisorption. Second, the H/Rh ratio was consistently lower on the bimetallic samples indicating that molybdena exerts a direct influence on the ability of supported Rh to chemisorb $H_2$ at room temperature.

Room-temperature chemisorption of CO quantitatively implies gem-dicarbonyl adsorption on both the bimetallic samples and on the most highly dispersed of the monometallic samples. As the Rh loading relative to the Mo loading becomes substantial, as in RhMo–IV, the stabilizing influence of Mo is diminished, so that the CO/Rh no longer reflects a dicarbonyl adsorption mode for CO. More importantly, the active site density on the bimetallic catalysts, as measured by CO chemisorption is similar to that on the monometallic catalysts of equivalent loading. So, rather than some molybdena decoration of Rh aggregates which might have been divined by the $H_2$ chemisorption data, the Rh appears to be oxidatively

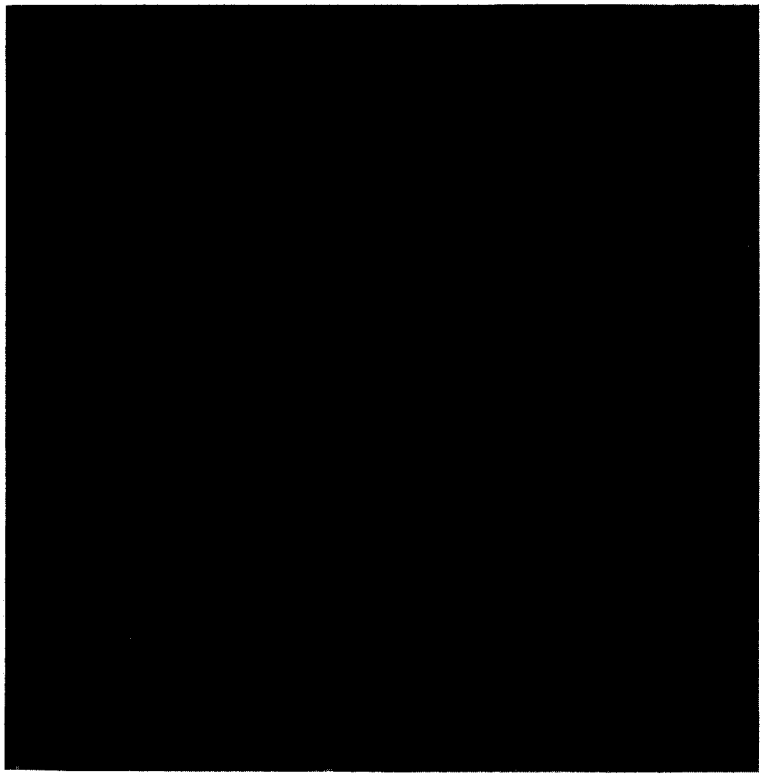

Fig. 11. RhMo–III after > 10 h on-stream for CO hydrogenation. Areas (A) and (C) depict regions of the alumina support and area (B) depicts a region of high contrast associated with transition-metal enrichment.

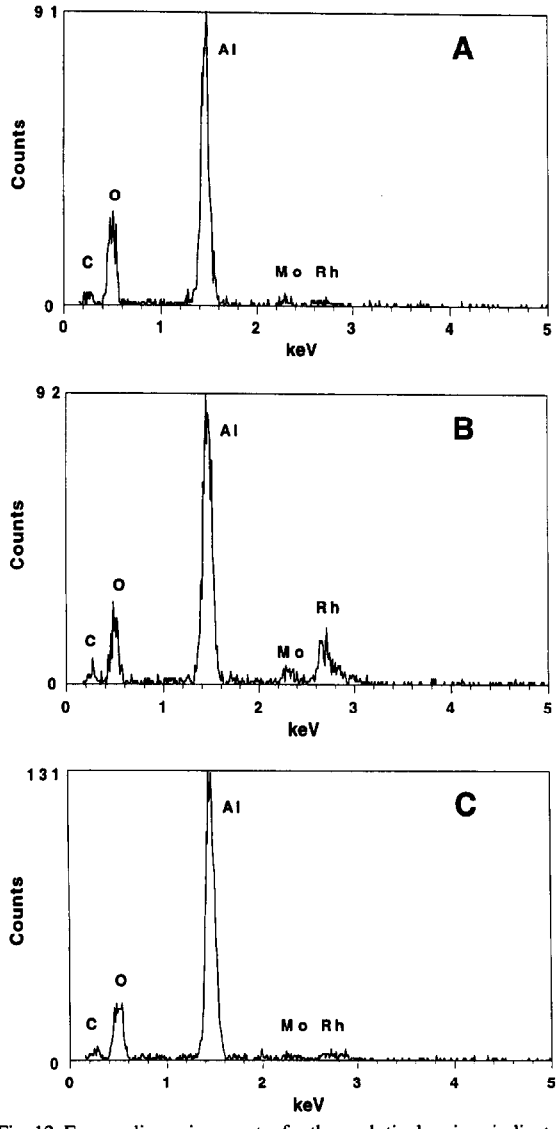


Fig. 12. Energy dispersive spectra for the analytical regions indicated in Fig. 11: (A) and (C) are alumina support and (B) contains the additional X-ray signatures for the presence of both Rh and Mo.

linked to the molybdena, enhancing the stability of dicarbonyls but impairing rhodium's ability to chemisorb $H_2$.

HRTEM and associated EDS and FFT analysis address, most directly, the 'state of the supported components' on the catalysts evaluated in this investigation. Imaging and analysis suggest that ordered Rh aggregates are present on both the unpromoted and Mo-promoted samples after extended CO hydrogenation testing. These Rh aggregates are less prevalent and smaller on the bimetallic samples, supporting the contention that molybdena kinetically stabilizes Rh against reductive agglomeration through gem-dicarbonyl migration. In addition, amorphous regions of transition metal enrichment containing both Rh and Mo were common on the bimetallic samples. These disordered domains of intimate contact between Rh and molybdena represent surface structures where oxidatively stabilized Rh, fingerprinted by our chemisorption analysis, could be present. Finally, while it was possible to image and evaluate isolated Rh crystallites on the bimetallic surface, there was no evidence with HRTEM for the decoration of these aggregates by a molybdena adlayer following prolonged CO hydrogenation testing.

### 4.2. *Unifying observations*

Our characterization efforts point to both kinetic stabilization of Rh by molybdena and an oxidative interaction between molybdena and Rh which stabilizes $Rh(I)(CO)_2$ species on the catalyst surface. Fig. 14 suggests a molecular representation of molybdena's stabilizing influence on active Rh centers. While we argue against the mechanism of molybdenum oxide migration and associated grafting on Rh aggregates, some comments are appropriate regarding where this investigation falls on the role of Mo. Such comments are particularly apt in light of the evidence from other laboratories, alluded to in the Introduction, which supports the metal–oxide migration and decoration paradigm. Table 5 organizes the Rh–Mo catalysts investigated by various research groups according to (i) the predominant explanation offered for the role of Mo, (ii) the transition-metal precursors used, (iii) the catalyst support employed, and (iv) the ultimate loadings of Rh and Mo. The trends highlighted by the Table 5 may explain some of the apparent discrepancies between theories adopted by the various groups.

The investigations which propose the kinetic stabilization of Rh aggregates against reductive agglomeration through gem-dicarbonyl migration

Fig. 13. FFT analysis of the amorphous region of transition-metal enrichment on RhMo–III depicted in Fig. 11 and confirmed by EDS to contain both Rh and Mo.

share several key features. First, they rely on experimental evidence which suggests a close proximity of Rh and Mo. As has been suggested previously [20], this close proximity may have been accentuated by the relative parity in Rh and Mo loading which was used to synthesize the catalysts which are associated with this model. Second, all of the studies referred to in this section of Table 5 employ organometallic precursors which have been chemisorbed on the catalyst support from an organic solvent. Research in our laboratories suggests that Mo carbonyls chemically interact with non-acidic hydroxyl sites on $Al_2O_3$ [22]. Furthermore, in the course of synthesizing Rh–Mo/$Al_2O_3$ of various loadings, we have repeatedly observed that a chemisorptive preparation sequence calculated to produce 6 wt% Mo/$Al_2O_3$ led, instead, to $\leq 3$ wt% Mo loading even after extended reflux of the $Mo(CO)_6$, $Al_2O_3$, and heptane slurry. Presumably, a similar *chemisorptive* limit for Mo exists on the surface of $SiO_2$.

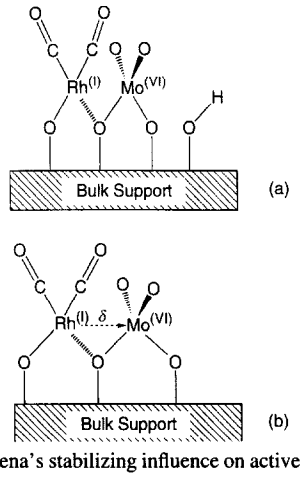


Fig. 14. Molybdena's stabilizing influence on active Rh centers: (a) inhibition of hydroxyl-mediated gem-dicarbonyl migration (i.e. kinetic stabilization) and (b) oxidative stabilization of gem-dicarbonyl surface moieties.

This chemisorptive Mo limit of $\sim 3$ wt% has been exceeded considerably in several of the samples associated with the metal–oxide migration model (at least on $Al_2O_3$). In addition, these materials were synthesized via aqueous impregnation of the porous supports, followed by subsequent calcination in air. While the calcination step, no doubt, promotes the chemical interaction of the transition-metals ions with the support, some

Table 5
Catalysts behind the three paradigms for the role of Mo in alumina- and silica-supported Rh

| Paradigm | Precursors | Support [a] | Rh wt% | Mo wt% | Ref. |
|---|---|---|---|---|---|
| I. Kinetic stabilization | $Cp_3RhMo_2(CO)_5$ | $SiO_2$ | 1.4 | 2.5 | [8,12] |
| | $Rh(CO)_2(acac)$, $Mo(CO)_6$ | $Al_2O_3$ | 3.0 | 2.8 | [10] |
| | $Rh_4(CO)_{12}$, $Mo(CO)_6$ | $SiO_2$ | 1.0 | 0.9 | [15] |
| | $Rh(CO)_2(acac)$, $Mo(CO)_6$ | $Al_2O_3$ | 0.2–2.4 | 1.2–1.5 | [20] |
| | $RhMo(CO)_3Cp(PPh_3)_2$ | $Al_2O_3$, $SiO_2$ | 0.5–0.6 | 0.5–0.7 | [21] |
| | $RhH(CO)(PPh_3)_3$, $[Mo(CO)_3Cp]_2$ | $Al_2O_3$, $SiO_2$ | 0.3–0.4 | 0.4 | [21] |
| II. Metal–oxide migration | $Rh(NO_3)_3$, $(NH_4)_6Mo_7O_{24}\cdot 4H_2O$ | $SiO_2$ | 1.5 | 1.4–5.5 | [5] |
| | $Rh(NO_3)_3$, $(NH_4)_6Mo_7O_{24}\cdot 4H_2O$ | $Al_2O_3$ | 3.0 | 7.5&15 | [6] [b] |
| | $RhCl_3$, $(NH_4)_6Mo_7O_{24}\cdot 4H_2O$ | $SiO_2$ | 1.6&2.3 | 3.0&4.1 | [8] |
| | $Rh(NO_3)_3$, $(NH_4)_6Mo_7O_{24}\cdot 4H_2O$ | $Al_2O_3$ | 1.0 | 3.0–12 | [11] |
| | $Rh_4(CO)_{12}$, $(NH_4)_6Mo_7O_{24}\cdot 4H_2O$ | $SiO_2$ | 1.0 | 0.5–5.0 | [19] |
| III. Oxidative stabilization | $RhCl_3$, $(NH_4)_6Mo_7O_{24}\cdot 4H_2O$ | $SiO_2$ | 1.6&2.3 | 3.0 | [8] |
| | $Cp_3RhMo_2(CO)_5$ | $SiO_2$ | 1.4 | 2.5 | [13] |
| | $Rh_4(CO)_{12}$, $(NH_4)_6Mo_7O_{24}\cdot 4H_2O$ | $SiO_2$ | 1.0 | 0.5–5.0 | [19] |

[a] Other more basic supports were also examined in several of these studies.
[b] The promoter-effect model in this investigation was proposed to be the activation of $H_2$ by the reduction of $MoO_3$.

domains of isolated $MoO_3$ may have been formed which were only tenuously anchored to the support surface. These loosely anchored domains of $MoO_3$, rather than serving to isolate Rh in an array of small aggregates, may migrate across the support surface under the reductive influence of $H_2$ during CO hydrogenation. While we have presented no direct experimental evidence for these distinct $MoO_x$ surface species *in metal-salt derived materials*, the work of Shen and coworkers [19] distinguishes between two different CO adsorption regimes determined by Mo loading on silica-supported Rh–Mo — below 1% and from 1–5% Mo.

Shen and coworkers also evoke the idea that intimate contact between the Rh and Mo is necessary for the oxidative stabilization of $Rh^{+1}$ species, and they point out that such oxidative interactions may occur prior to CO exposure. Trunschke and coworkers directly compare the behavior of salt-derived and heteronuclear, organometallic-derived Rh–Mo catalysts in terms of their behavior in the presence of CO and find evidence for a dative electron interaction between molybdena and $Rh^{+1}$ for the salt-derived materials [8]. Later investigations on the heteronuclear, organometallic-derived Rh–Mo catalysts associate these materials with both the kinetic stabilization of Rh through bimetallic alloy formation [12] and the oxidative stabilization of Rh carbonyls, which, they suggested, enhances CO insertion [13].

As these observations imply, the three paradigms for Mo promotion are not necessarily incompatible. In particular, a close proximity of molybdena and Rh may lead to both kinetic and oxidative stabilization of small Rh aggregates. Furthermore, the migration of molybdena may only be significant above its chemisorptive limit on a particular support medium. Below this limit, enhancement of oxygenate selectivity in the Rh–Mo system may simply be a combination of chemical and textural promotion, without decoration of Rh aggregates.

## Acknowledgements

Assistance from Dr. Theodore A. Nolan, Manager of the Materials Analysis User Center, in facilitating research conducted at ORNL is acknowledged with thanks. Support for this research was provided by the Pittsburgh Energy and Technology Center under the auspices of the

Department of Energy, University Coal Research Program, Grant No. DE-F622-90PC90291. Additional support for travel and direct access to electron microscopy facilities at ORNL was provided by the Oak Ridge Institute for Science and Education (ORISE) and the Department of Energy, Assistant Secretary for Energy Efficiency and Renewable Energy, Office of Transportation Technologies, as part of the High Temperature Materials Laboratory User Program, under contract DE-AC05-84OR211400 with Martin Marietta Energy Systems, Inc. (a division of Lockheed Martin).

## References

[1] Y.I. Yermakov, B.N. Kuznetsov and E.M. Chalganov, React. Kinet. Catal. Lett., 14 (1980) 37.
[2] B.N. Kuznetsov and E.M. Chalganov, React. Kinet. Catal. Lett., 18 (1981) 213.
[3] M. Ichikawa, T. Fukushima and K. Shikakura, Proc. 8th Int. Congr. Catal., Berlin, Vol. II (1984) 69.
[4] F.G.A. van den Berg, J.H.E. Glezer and W.M.H. Sachtler, J. Catal., 93 (1985) 340.
[5] B.J. Kip, E.G.F. Hermans, J.H.M.C. van Wolput, N.M.A. Hermans, J. van Grondelle and R. Prins, Appl. Catal., 35 (1987) 109.
[6] N.A. Bhore, C. Sudhakar, K.B. Bischoff, W.H. Manogue and G.A. Mills, Proc. 9th Int. Congr. Catal., Ottawa, Vol. 2 (1988) 594.
[7] R.P. Underwood and A.T. Bell, J. Catal., 111 (1988) 325.
[8] A. Trunschke, H. Ewald, D. Gutschick, H. Miessner, M. Skupin, B. Walther and H.-C. Böttcher, J. Mol. Catal., 56 (1989) 95.
[9] B. Walther, M. Scheer, H.-C. Böttcher, A. Trunschke, E. Ewald, D. Gutschick, H. Miessner, M. Skupin and G. Vorbeck, Inorg. Chim. Act., 156 (1989) 285.
[10] H.C. Foley, A.J. Hong, J.S. Brinen, L.F. Allard and A.J. Garratt-Reed, Appl. Catal., 61 (1990) 351.
[11] E.C. Decanio and D.A. Storm, J. Catal., 132 (1991) 375.
[12] R. Lambert, N.I. Jaeger, A. Trunschke and H. Miessner, Catal. Lett., 11 (1991) 1.
[13] A. Trunschke, H. Ewald, H. Miessner, A. Fukuoka, M. Ichikawa and H.-C. Böttcher, Mater. Chem. Phys., 29 (1991) 503.
[14] T. Koerts, W.J.J. Welters and R.A. van Santen, J. Catal., 134 (1992) 1.
[15] A. Trunschke, H. Ewald, H. Miessner, S. Marengo, S. Martinengo, F. Pinna and L. Zanderighi, J. Mol. Catal., 74 (1992) 365.
[16] J.P. Hindermann, G.J. Hutchings and A. Kiennemann, Catal. Rev.-Sci. Eng., 35 (1993) 1.
[17] O.S. Alekseev, T. Beutel, E.A. Paukshtis, Y.A. Ryndin, V.A. Likholobov and H. Knözinger, J. Mol. Catal., 92 (1994) 217.
[18] A.L. Borer, C. Brönnimann and R. Prins, J. Catal., 145 (1994) 516.
[19] J.Y. Shen, T. Matsuzaki, T. Hanaoka, K. Takeuchi and Y. Sugi, Catal. Lett., 28 (1994) 329.
[20] M. Te, E.E. Lowenthal and H.C. Foley, Chem. Eng. Sci., 49 (1994) 4851.
[21] M. Te, E.E. Lowenthal and H.C. Foley, J. Catal., 146 (1994) 591.
[22] E.E. Lowenthal and H.C. Foley, J. Catal., 155 (1995) in press.
[23] C.E. Scott, T. Romero, E. Lepore, M. Arruebarrena, P. Betancourt, C. Bolívar, M.J. Pérez-Zurita, P. Marcano and J. Goldwasser, Appl. Catal. A, 125 (1994) 71.
[24] A.K. Datye and D.J. Smith, Catal. Rev.–Sci. Eng., 34 (1992) 129.
[25] R.W. Horne and R. Markham, in A.M. Glauert (Ed.), Practical Methods in Electron Microscopy, Vol. 1, North-Holland Publishing Company, Amsterdam, 1972, p. 327.
[26] A. Reeves, FFT Extension to Image 1.25, Public Domain Software Documentation, Dartmouth College (1990).
[27] S. Cao and L.F. Allard, Lattice Fringe Space Measurement Using Fourier Transform in Digitized HRTEM Image, to be submitted, (1995).
[28] C. Wong and R.W. McCabe, J. Catal., 119 (1989) 47.
[29] F. Solymosi and M. Pásztor, J. Phys. Chem., 89 (1985) 4789.
[30] F. Solymosi and M. Pásztor, J. Phys. Chem., 90 (1986) 5312.
[31] M.D. Wardinsky and W.C. Hecker, J. Phys. Chem., 92 (1988) 2602.
[32] T.H. Ballinger and J.T. Yates, Jr., J. Phys. Chem., 95 (1991) 1694.
[33] M.I. Zaki, G. Kunzmann, B.C. Gates and H. Knözinger, J. Phys. Chem., 91 (1987) 1486.
[34] M.P. Keyes and K.L. Watters, J. Mol. Catal., 52 (1989) 253.
[35] M.I. Zaki, T.H. Ballinger and J.T. Yates, Jr., J. Phys. Chem., 95 (1991) 4028.
[36] D.K. Paul and J.T. Yates, Jr., J. Phys. Chem., 95 (1991) 1699.
[37] B.E.P. Beeston, in A.M. Glauert (Ed.), Practical Methods in Electron Microscopy, Vol. 1, North-Holland Publishing Company, Amsterdam, 1972, p. 192.
[38] A.D. Logan, Braunschweig, A.K. Datye and D.J. Smith, Langmuir, 4 (1988) 827.